



Cite as
Nano-Micro Lett.
(2023) 15:207

Received: 30 May 2023
Accepted: 15 July 2023
© The Author(s) 2023

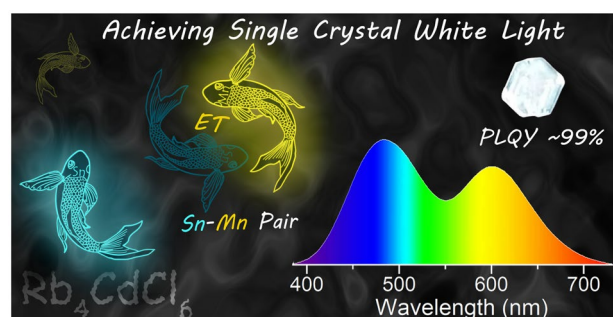
Achieving Tunable Cold/Warm White-Light Emission in a Single Perovskite Material with Near-Unity Photoluminescence Quantum Yield

Bo Zhou^{1,2}, Aixuan Du¹, Dong Ding², Zexiang Liu¹, Ye Wang³, Haizhe Zhong¹, Henan Li⁴, Hanlin Hu⁵ ✉, Yumeng Shi⁴ ✉

HIGHLIGHTS

- High-quality Sn²⁺/Mn²⁺-co-doped Rb₄CdCl₆ single crystals and powders were prepared and showed high-performance dual-emission white light with near-unity photoluminescence quantum yield.
- Short-range and extremely strong interactions between Sn²⁺ and Mn²⁺ were observed that lead to an intriguing ultra-high-efficiency Dexter energy transfer process from adjacent Sn²⁺ ions to Mn²⁺ ions.
- The dual-emission intensities were tuned flexibly by varying the fractions of Sn²⁺ and Sn–Mn pairs to balance their emission proportions for cold/warm white-light generation.

ABSTRACT Single materials that exhibit efficient and stable white-light emission are highly desirable for lighting applications. This paper reports a novel zero-dimensional perovskite, Rb₄CdCl₆:Sn²⁺, Mn²⁺, which demonstrates exceptional white-light properties including adjustable correlated color temperature, high color rendering index of up to 85, and near-unity photoluminescence quantum yield of 99%. Using a co-doping strategy involving Sn²⁺ and Mn²⁺, cyan-orange dual-band emission with complementary spectral ranges is activated by the self-trapped excitons and *d-d* transitions of the Sn²⁺ and Mn²⁺ centers in the Rb₄CdCl₆ host, respectively. Intriguingly, although Mn²⁺ ions doped in Rb₄CdCl₆ are difficult to excite, efficient Mn²⁺ emission can be realized through an ultra-high-efficient energy transfer between Sn²⁺ and Mn²⁺ via the formation of adjacent exchange-coupled Sn–Mn pairs. Benefiting from this efficient Dexter energy transfer process, the dual emission shares the same optimal excitation wavelengths of the Sn²⁺ centers and suppresses the non-radiative vibration relaxation significantly. Moreover, the relative intensities of the dual-emission components can be modulated flexibly by adjusting the fraction of the Sn²⁺ ions to the Sn–Mn pairs. This co-doping approach involving short-range energy transfer represents a promising avenue for achieving high-quality white light within a single material.



adjacent exchange-coupled Sn–Mn pairs. Benefiting from this efficient Dexter energy transfer process, the dual emission shares the same optimal excitation wavelengths of the Sn²⁺ centers and suppresses the non-radiative vibration relaxation significantly. Moreover, the relative intensities of the dual-emission components can be modulated flexibly by adjusting the fraction of the Sn²⁺ ions to the Sn–Mn pairs. This co-doping approach involving short-range energy transfer represents a promising avenue for achieving high-quality white light within a single material.

KEYWORDS 0D perovskite; Multi-ion doping; Near-unity white light; Energy transfer; Self-trapped excitons

Bo Zhou and Aixuan Du have contributed equally to this work.

✉ Hanlin Hu, hanlinhu@szpt.edu.cn; Yumeng Shi, yumeng.shi@szu.edu.cn

¹ International Collaborative Laboratory of 2D Materials for Optoelectronics Science and Technology of Ministry of Education, Institute of Microscale Optoelectronics, Shenzhen University, Shenzhen 518060, People's Republic of China

² Shandong Laboratory of Yantai Advanced Materials and Green Manufacturing, Yantai 264006, People's Republic of China

³ Key Laboratory of Material Physics, School of Physics and Microelectronics, Zhengzhou University, Ministry of Education, Zhengzhou 450052, People's Republic of China

⁴ School of Electronics and Information Engineering, Shenzhen University, Shenzhen 518060, People's Republic of China

⁵ Hoffmann Institute of Advanced Materials, Shenzhen Polytechnic, Shenzhen 518060, People's Republic of China

Published online: 31 August 2023



SHANGHAI JIAO TONG UNIVERSITY PRESS

Springer

1 Introduction

Metal halide perovskites, specifically those containing self-trapped excitons (STEs), have garnered significant attention as promising candidates for white-light-emitting diodes (WLEDs) because of their ultra-broadband emission characteristics and high photoluminescence quantum yields (PLQYs) [1–9]. The ability to emit light across the entire visible spectrum enables the realization of white light from a single emitter layer, simplifying device fabrication [3, 10]. While achieving high efficiency is crucial, it is equally important to attain a high color render index (CRI) and adjustable correlated color temperature (CCT) for applications that require high-quality and color-critical lighting, such as art galleries, photography, surgery, and military signs [11–13]. However, meeting these requirements using a single broadband emission source poses significant challenges [14].

Integrating auxiliary emission channels or components with different emission wavelengths into the broadband emission is an effective strategy to improve CRI and adjust CCT [15, 16]. While the assembly of multi-band emissions from chemically similar and coexisting perovskite materials has led to the successful realization of high-quality white light, coordinating different emissions within a single material offers distinct advantages. This design approach avoids color instability caused by different degradation rates of the emitters and minimizes efficiency losses due to emission reabsorption [17]. Generally, in metal halide perovskite materials, the $[BX_6]^{n-}$ octahedra serve as the fundamental functional units, and the interactions between these units dictate the material's physical properties [18, 19]. Leveraging the structural tolerance of perovskite materials, different kinds of $[BX_6]^{n-}$ octahedra can be assembled in a single material to achieve various optical properties [20–23]. Recently, the integration of hybrid B-site metals has enabled the realization of multiple emission channels with individually tuned wavelengths and the achievement of high-quality white-light within a single perovskite material [24–29].

All-inorganic perovskites offer advantages in terms of stability against heat and UV radiation compared to hybrid organic–inorganic perovskites, which are prone to

photobleaching and aging of organic functional groups [3, 30]. However, the complex interactions between identical and different $[BX_6]^{n-}$ octahedra within a compact lattice should be carefully considered. For example, all-inorganic perovskites often exhibit low intrinsic PL intensity due to the indirect bandgap and significant concentration quenching [31]. Achieving efficient broadband STEs emission requires appropriate dilution of ns^2 ions (i.e., ions that have outermost s^2 electrons, such as Pb^{2+} , Sn^{2+} , Sb^{3+} , Bi^{3+} , Te^{4+}) into a host material with large bandgap [32]. Incorporation of additional optical dopant centers to generate auxiliary emissions without significant quenching of the overall PLQY remains a challenge [17]. Successful achievement of efficient and tunable white light in a single all-inorganic perovskite has been demonstrated in 2021, such as co-doping Sb^{3+} and Bi^{3+} in $Cs_2NaInCl_6$ [24]. Over the years, various combinations of optical dopants have been developed, including Sb^{3+}/Bi^{3+} -co-doped Cs_2SnCl_6 [25], Bi^{3+}/Te^{4+} -co-doped Cs_2SnCl_6 [26, 27], and Sb^{3+} -doped Cs_2ZrCl_6 [28, 29]. However, these different emission sources often require distinct optimal excitation ranges. Finding a common excitation wavelength that aligns with the optimal excitations of each emission source remains challenging, leading to unstable color rendering and significant efficiency losses.

Energy-transfer-related fluorescence between ns^2 ion sensitizers and Ln^{3+}/TM^{n+} (Ln : lanthanides, TM : transition metals) ion activators enable the emission from TM^{n+} centers to possess the same excitation profile as STEs emission from the ns^2 centers [33]. In our previous work, we incorporated rare-earth Er^{3+} and Ho^{3+} ions with Sb^{3+} in $Cs_2NaInCl_6$ host, demonstrating the feasibility of achieving tunable white-light via an energy transfer design [34]. The Er^{3+} , Ho^{3+} optical centers exhibited sharp-band green and red emission sensitized by Sb^{3+} , with an identical excitation profile to the primary broadband blue emission. While the sharp-band emission from rare earths efficiently adjusted the CCT, they contributed minimally to the improvement of CRI. Mn^{2+} ions were considered as a more suitable alternative to co-doped with ns^2 ions compared to Ln^{3+} ions, owing to the broadband emission from $d-d$ transition [35]. Despite the ease of constructing energy transfer between ns^2 ions and Mn^{2+} , achieving efficient white light has remained a challenge [36–39]. Dexter energy transfer

is short-range interaction which moves an exciton (i.e., an electron–hole pair) from a donor to an acceptor [40]. The free excitons generated by ns^2 ions in the metal halides lattice upon photon absorption possess the potential to form DET pairs with Ln^{3+}/TM^{n+} ions and thereby enhance the optical properties. However, the Dexter energy transfer has rarely been observed in metal halides.

In this work, we selected the broadband cyan STEs emission in Sn^{2+} -doped Rb_4CdCl_6 as the primary emission. Through further co-doping of Mn^{2+} , a typical short-range Dexter energy transfer from Sn^{2+} to Mn^{2+} was generated, which not only produced an additional orange broadband emission for high-quality dual-emission white light but also enhanced the total PLQY to near-unity. The dual-emission shows almost the same excitation spectra originate from Sn^{2+} ions, and their relative intensities can be continuously tuned by the fractions of Sn^{2+} and Sn – Mn pairs to balance their emission proportions for cold/warm white-light generation.

2 Experimental Section

2.1 Materials

$RbCl$ (99.99% metals basis), $CdCl_2$ (anhydrous, 99.99% metals basis), $SnCl_2 \cdot 2H_2O$ (99.99% metals basis), hypophosphorous acid (H_3PO_2 , 50 wt% in H_2O), isopropanol (IPA, AR), and dimethylformamide (DMF, AR) were purchased from Aladdin. $MnCl_2 \cdot 4H_2O$ (99% metals basis) was purchased from Alfa Aesar. Hydrochloric acid (HCl, AR) was purchased from Guangzhou Chemical Reagent Factory. All chemicals were used as received without any further purification.

2.2 Preparation of Single Crystal, Powder, and LEDs

2.2.1 Preparation of Sn^{2+} , Mn^{2+} , and Sn^{2+}/Mn^{2+} -Co-Doped Rb_4CdCl_6 Powders

1 mmol (0.121 g) of $RbCl$ was dissolved in 1 mL of HCl to prepare a 1 M $RbCl$ solution. 2 mmol (0.367 g) of $CdCl_2$ was dissolved in 1 mL of HCl to prepare a 2 M $CdCl_2$ solution. 0.1 mmol (0.023 g) of $SnCl_2 \cdot 2H_2O$ was dissolved in a mixture of 1 mL of HCl and 0.1 mL of H_3PO_2 to prepare a 0.1 M $SnCl_2$ solution. 1 mmol (0.198 g) of $MnCl_2 \cdot 4H_2O$ was dissolved in 1 mL of HCl to prepare a 1 M $MnCl_2$

solution. The $CdCl_2$ solution (0.5 mL) was premixed with IPA (5 mL), and then, the $RbCl$ solution (4 mL) was rapidly injected into the mixture to obtain pure Rb_4CdCl_6 precipitation. To obtain the Sn^{2+} (or Mn^{2+})-doped Rb_4CdCl_6 samples, $SnCl_2$ (or $MnCl_2$) solution should be added to the $CdCl_2$ solution while maintaining a total amount of $SnCl_2$ (or $MnCl_2$) and $CdCl_2$ of 1 mmol [$M^{II}/(M^{II} + Cd) \times 100\%$]. All precipitations were dried at 50 °C for 30 min.

2.2.2 Growth of Sn^{2+}/Mn^{2+} -Co-Doped Rb_4CdCl_6 Single Crystals

The synthesis of the Sn^{2+}/Mn^{2+} -co-doped Rb_4CdCl_6 single crystal was based on a hydrothermal method. First, 16 mmol of $RbCl$, 4 mmol of $CdCl_2$, 0.8 mmol of $SnCl_2$, and 0.8 mmol of $MnCl_2$ were added to a 25-mL Teflon liner. Then, 8 mL of HCl, 8 mL of DMF, and 0.8 mL of H_3PO_2 were injected into the Teflon liner. The Teflon liner was sealed in a stainless-steel autoclave and then was heated to 120 °C for 10 h. The reaction mixture was subsequently cooled to room temperature at a rate of 3 °C h^{-1} . Finally, the samples were cleaned with IPA and dried at 50 °C for 30 min.

2.2.3 Fabrication of Down-Conversion WLEDs

One gram of the Sn^{2+}/Mn^{2+} -co-doped Rb_4CdCl_6 powder sample was dispersed into 1 g of organic silicone, and then, the gel mixture obtained was cast on the surface of an LED chip (purchased from Shenzhen Ruibaoguang Technology Co., Ltd.) with an emission wavelength of 295 nm. Finally, the LEDs obtained by this method were dried at 80 °C for 24 h in a vacuum drying chamber.

2.3 Characterization

Powder X-ray diffraction (XRD) measurements were taken using a D2 diffractometer (Bruker, Billerica, MA, USA) with $Cu K\alpha$ radiation ($\lambda = 1.5418 \text{ \AA}$). Energy-dispersive X-ray spectroscopy (EDS) characterization of the microcrystal was performed using a field-emission scanning electron microscope (FESEM; SU8010, Hitachi). UV–visible absorption spectroscopy was performed using a UV–Vis–near-infrared (NIR) spectrometer (UV-2600i, Shimadzu, Kyoto, Japan). The photoluminescence (PL), photoluminescence excitation

(PLE) spectra, and PLQY measurements were taken using a fluorescence spectrophotometer (FS5, Edinburgh Instruments, Livingston, UK). The time-resolved PL spectroscopy measurements were also taken using the FS5 fluorescence spectrometer with a microsecond lamp acting as its excitation source. Inductively coupled plasma optical emission spectroscopy (ICP-OES) was performed using an atomic emission spectrometer (JY2000-2, Horiba, Japan). The zero-field-cooled (ZFC) and field-cooled (FC) curve measurements were taken using an integrated physical property measurement system (PPMS-9 T, Quantum Design, USA). Electron paramagnetic resonance (EPR) characterization was performed using an electronic paramagnetic resonance spectrometer (EPR200-Plus, Chinainstru & Quantumtech (CIQTEK), China). The PL spectra of the LED for different drive currents were measured using a ScanPro Advance system (Metatest, China).

3 Results and Discussion

The crystal structure of Rb_4CdCl_6 is illustrated in Fig. 1a, exhibiting a characteristic zero-dimensional (0D) crystal structure with trigonal $R\bar{3}c$ symmetry, resembling that of Cs_4PbBr_6 [41]. In this structure, the $[\text{CdCl}_6]^{4-}$ octahedra are completely isolated by Rb^+ ions [42]. Substituting Cd^{2+} ions with Sn^{2+} and Mn^{2+} ions lead to the formation of $[\text{SnCl}_6]^{4-}$ and $[\text{MnCl}_6]^{4-}$ octahedra, respectively, as they have comparable radii and the same divalent charge as Cd^{2+} . An optical image of a single crystal of $\text{Sn}^{2+}/\text{Mn}^{2+}$ -co-doped Rb_4CdCl_6 prepared via a hydrothermal method is shown in Fig. 1b [43]. The crystal appears colorless under daylight, due to the extremely weak absorption of Mn^{2+} ions doping in Rb_4CdCl_6 (Fig. S1), which distinguishes it from most of Mn^{2+} -doped/based perovskites [35, 44–46]. However, under UV light, the crystal emits bright white light, in contrast to the cyan emission of Sn^{2+} -doped Rb_4CdCl_6 [43], confirming the successful incorporation Mn^{2+} ions into the Rb_4CdCl_6 . Figure 1c shows the powder X-ray diffraction (PXRD) pattern of as-prepared Sn^{2+} and Mn^{2+} -co-doped Rb_4CdCl_6 samples. The observed PXRD patterns match well with the standard powder diffraction file [PDF 77–0871]. It is worth noting that Sn^{2+} and Mn^{2+} ions have larger and smaller ion radii ($r = 1.12$ and 0.83 Å, coordination number (CN) = 6), respectively, compared to Cd^{2+} ions ($r = 0.95$ Å, CN = 6), and the co-doping of Sn^{2+} and Mn^{2+} would offset

each other's influence on the cell volume. Scanning electron microscopy (SEM) with energy-dispersive spectral mapping (EDS mapping) was employed to analyze the samples. Figure 1d shows that Sn^{2+} and Mn^{2+} dopants are uniformly distributed in the microcrystal, confirming the successful preparation of the co-doped samples. Inductively coupled plasma optical emission spectroscopy (ICP-OES) was utilized to determine the doping ratio of Sn^{2+} and Mn^{2+} in the samples, considering both fixed and varying feed ratios of Sn^{2+} and Mn^{2+} . As depicted in Fig. S2, the actual amount of Sn^{2+} is $\sim 4.5\%$ in the different samples, slightly lower than the 5% feeding ratio. The actual amount of Mn^{2+} also aligns with the feed ratio due to homovalent substitution.

The introduction of Mn^{2+} ions into $\text{Rb}_4\text{CdCl}_6:\text{Sn}^{2+}$ results in an additional broadband emission component in the yellow–red region (denoted by as Mn_{Em}). Figure 2a shows a pseudo-color map of PL and PL excitation (PLE) for a sample with an Sn^{2+} and Mn^{2+} doping ratio of 4.5% and 3.4%, respectively. The PLE distribution pattern for the two emission components is similar, indicating that the design of the energy transfer from $[\text{SnCl}_6]^{4-}$ to $[\text{MnCl}_6]^{4-}$ had been achieved successfully. Figure 2b displays the emission profiles under excitation at 300 nm. Notably, the profile

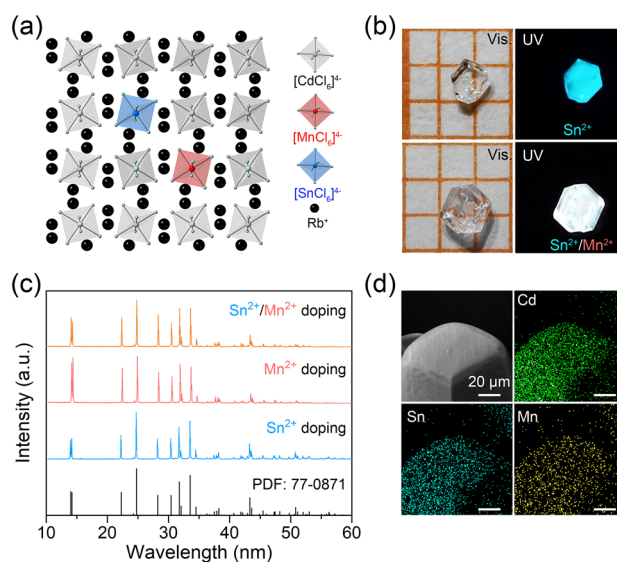


Fig. 1 a Schematic diagram of Rb_4CdCl_6 crystal structure and substitutions performed via Sn^{2+} and Mn^{2+} co-doping. b Optical images of Sn^{2+} -doped and $\text{Sn}^{2+}/\text{Mn}^{2+}$ -co-doped single crystals under daylight and UV light illumination. c Powder XRD patterns of Sn^{2+} , Mn^{2+} , and $\text{Sn}^{2+}/\text{Mn}^{2+}$ -co-doped Rb_4CdCl_6 samples; PDF 77-0871 is shown for comparison. d Energy-dispersive X-ray spectroscopy (EDS) mapping of the $\text{Sn}^{2+}/\text{Mn}^{2+}$ -co-doped Rb_4CdCl_6 microcrystal

of cyan emission component (485 nm) remains largely unchanged with the Mn^{2+} -co-doping, although its intensity decreases to 0.534 times that of the pristine emission in the Sn^{2+} -doped Rb_4CdCl_6 . Conversely, the extracted Mn_{Em} component (606 nm) exhibits a redshift of ~ 20 nm compared to the Mn^{2+} -doped Rb_4CdCl_6 (Fig. S3). These results can be attributed to the formation of Sn–Mn pairs, which involve a short-range and strong interaction between Sn^{2+} and Mn^{2+} ions. As a result, the Sn^{2+} dopants can be classified into two species: Sn^{2+} ions with and without the adjacent Mn^{2+} ions.

3.1 Analysis of Sn–Mn Dexter Energy Transfer Pair

As the PL excitation occurs in a fast process following the Franck–Condon approximation, from the ground state to the excited state, during which the surrounding lattice has no

chance to reorganize, the difference in the local environment of Sn^{2+} can be reflected by changes in the excitation spectrum. The PLE profiles corresponding to the Sn_{Em} and Mn_{Em} components (denoted by Sn_{Ex} and Mn_{Ex} , respectively) are carefully examined in Fig. 2d, e. In general, the PLE spectrum of ns^2 ion-doped perovskite exhibits a fine molecule-like structure resembling that of a molecule that consists of specific excitation bands [47, 48]. Peak fitting analysis using Gaussian function was performed to identify the origin of each band in the PLE spectra [48]. The Sn_{Ex} and Mn_{Ex} exhibit similar A and C bands ($^1S_0 \rightarrow ^3P_1$ and $^1S_0 \rightarrow ^1P_1$), but the bands in Mn_{Ex} have wider bandwidths compared to Sn_{Ex} , as listed in Table S1. In addition, a B band ($^1S_0 \rightarrow ^3P_2$), which is allowed by coupling with non-totally symmetric lattice vibrations, is observed in Mn_{Ex} . This suggests that the Sn^{2+} ions adjacent to Mn^{2+} ions experience a relatively

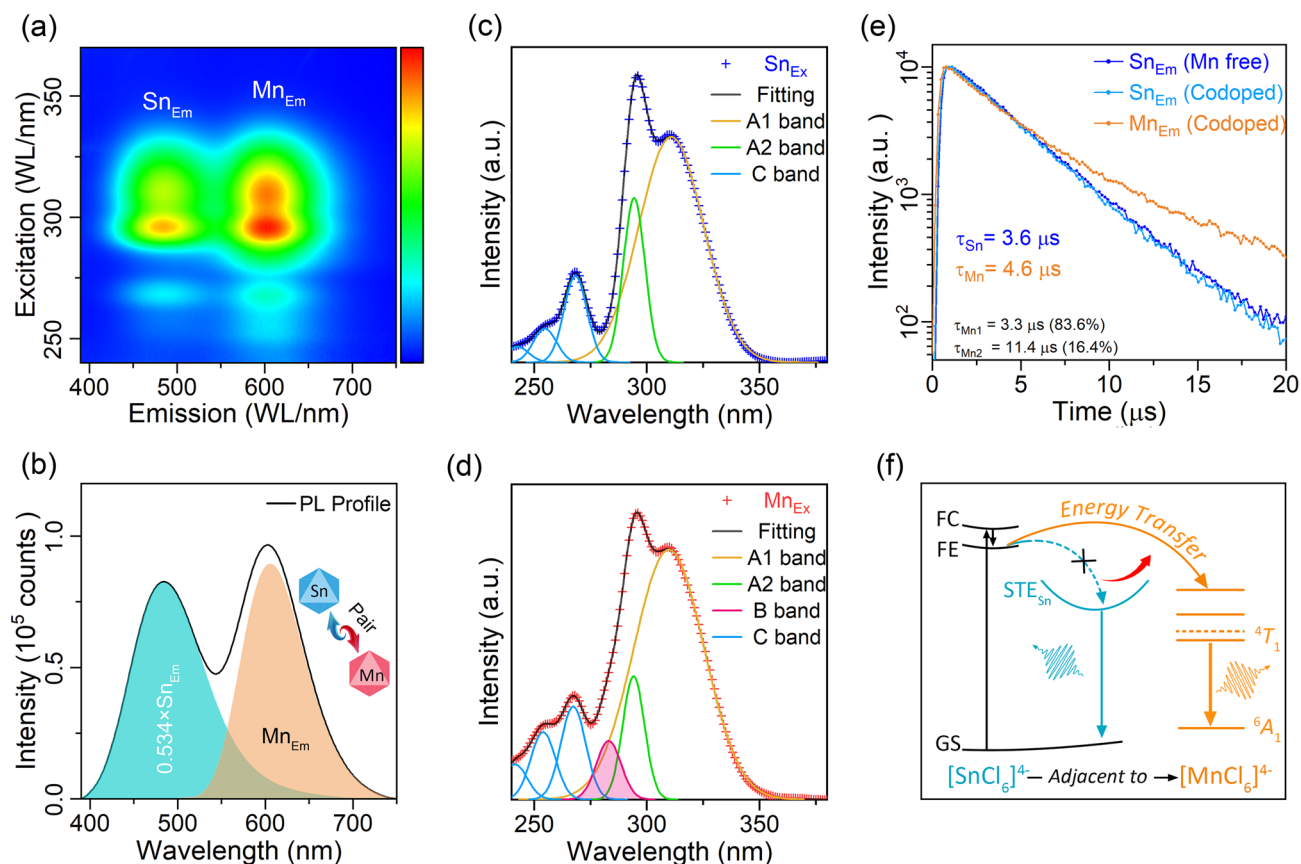


Fig. 2 **a** Pseudo-color map of the PL/PLE of $\text{Sn}^{2+}/\text{Mn}^{2+}$ -co-doped Rb_4CdCl_6 . **b** Dual-emission profile formed as a combination of two components, Sn_{Em} and Mn_{Em} . **c**, **d** Excitation profiles corresponding to Sn_{Em} and Mn_{Em} , respectively, consisting of A, B, and C bands. **e** Decay curves obtained for Sn_{Em} and Mn_{Em} at room temperature. **f** Schematic illustration of the energy transfer mechanism in the $\text{Sn}^{2+}/\text{Mn}^{2+}$ -co-doped Rb_4CdCl_6 system

distorted lattice environment, which can be attributed to the smaller ion radii Mn^{2+} .

The transient PL decay corresponding to Sn_{Em} and Mn_{Em} components was measured by excitation at C band (268 nm) at room temperature and is shown in Fig. 2e [48]. The decay curves of Sn_{Em} remained nearly unchanged with the co-doping of Mn^{2+} , confirming that the Sn^{2+} specie that without adjacent Mn^{2+} ions maintained their pristine cyan STEs emission and were not significantly influenced by Mn^{2+} co-doping. In contrast, the lifetime of the Mn_{Em} decreased dramatically from 6.4 (Fig. S4) to 4.6 μs , indicating that the parity-forbidden property of the 4T_1 to 6A_1 transition had been removed, further confirming the strong interaction between adjacent Sn^{2+} and Mn^{2+} ions. Moreover, the decay curve of Mn_{Em} component can be well described by a biexponential fit, with two lifetime constants of 3.3 and 11.4 μs , accounting for 86% and 14% of the total decay, respectively. Notably, the dominant short lifetime constant is shorter than the lifetime of the Sn_{Em} component (3.5 μs), indicating the energy transfer occurs from FE rather than STE states of Sn^{2+} ions. Previous studies have shown that in the presence of STEs [14], once electrons and holes are photogenerated, they quickly become self-trapped, resulting in a more stable state with lattice distortion. However, in the presence of adjacent Mn^{2+} ions, a more stable state is provided, and the photogenerated electrons and holes move to the Mn^{2+} center corresponding to a short-range exchange-coupled interaction instead of becoming self-trapped, as illustrated in Fig. 2f.

In Fig. 3a, the optical image of as-prepared $\text{Sn}^{2+}/\text{Mn}^{2+}$ -co-doped Rb_4CdCl_6 samples under UV light is shown, with a fixed doping rate of 4.5% for Sn^{2+} and varying from 0 to 40% for Mn^{2+} . The PL color gradually transitions from cyan to white and then to orange as the Mn^{2+} co-doping ratio increases. The corresponding PL spectra, collected using an integral sphere, are shown in Figs. 3b and S5. The intensity of Mn_{Em} component increases with the Mn^{2+} doping ratio until it reaches a maximum intensity at a co-doping ratio of 7.1 at%, while the intensity of the cyan emission continuously decreases. Figure S6 demonstrates that the extracted Mn_{Em} component from different samples exhibits an identical profile at 606 nm, which is unaffected by the amount of Mn^{2+} co-doping. The integral intensities of dual emissions are presented in Fig. 3c. It is noteworthy that an appropriate amount of Mn^{2+} co-doping (<7.1%) can improve the PLQY of the system from ~90% to near unity (>99%) (Fig. S7). However, further increase in the Mn^{2+} doping amount leads

to typical concentration-related quenching. To investigate the quenching processes, electron paramagnetic resonance (EPR) characterization was performed (Figs. S8 and S9). The EPR spectrum of $\text{Rb}_4\text{CdCl}_6:\text{Mn}^{2+}$ with and without Sn^{2+} co-doping exhibited a similar six-hyperfine lines profile, indicating the long-range Mn–Mn dipolar interaction was not significantly influenced by Sn^{2+} ions [36]. The broadening of the six-hyperfine lines is observed with increasing the Mn^{2+} content, indicating a decrease in the average distance between Mn–Mn centers [36]. As the Mn^{2+} doping ratio increases, the short-range exchange-coupled Mn–Mn interaction becomes dominant, leading to a significant quenching in PL [36]. This quenching process can be attributed to the competition between Mn–Mn and Sn–Mn exchange coupling interactions. The near-unity PLQY suggests that internal energy transfer efficiency from Sn^{2+} to Mn^{2+} is a high (see details in Supporting information), prioritizing over the formation of STE and non-radiative vibrational relaxation since excited Sn^{2+} serves as the sole energy source of Mn_{Em} . The combination of cyan Sn_{Em} and orange Mn_{Em} enables the creation of high-quality tunable cold/warm white light, where the relative intensity of the two components depends on the ratio of the two Sn^{2+} species, as follows:

$$\frac{I_{\text{Cyan}}}{I_{\text{Orange}}} = \frac{c_{\text{Res}}}{c_{\text{Pair}}} \times \frac{QY_{\text{STE}}}{QY_{\text{Mn}}} \quad (1)$$

where c_{Res} and c_{Pair} are the concentrations of the Sn^{2+} ion with and without adjacent Mn^{2+} ions and QY_{STE} and QY_{Mn} are the PL efficiencies of the cyan STE emission and the Mn^{2+} *d-d* emission, respectively. When the doping concentrations of Sn^{2+} and Mn^{2+} ions are relatively low, the values of QY_{STE} and QY_{Mn} are constant by approximation. Because short-range interactions occur between the Sn^{2+} and Mn^{2+} ions, Sn–Mn pairs arise when the Sn^{2+} and Mn^{2+} centers are less than a certain distance r apart. From a geometric crystallography perspective (Fig. S10), the fraction of the residual Sn^{2+} ions (without any adjacent Mn^{2+} ions) can be described as:

$$P_{\text{Res}} = \frac{c_{\text{Res}}}{c_{\text{Pair}} + c_{\text{Res}}} = (1 - \text{Mn}\%)^n \quad (2)$$

where n is the number of Cd^{2+} sites in a sphere with a Sn^{2+} ion as the center with a radius of r . According to Eqs. 1 and 2, the variation in the intensity of the Sn_{Em} component with Mn^{2+} content can be described as follows:

$$I_{\text{Res}} = I_0 \times (1 - \text{Mn}\%)^n \quad (3)$$

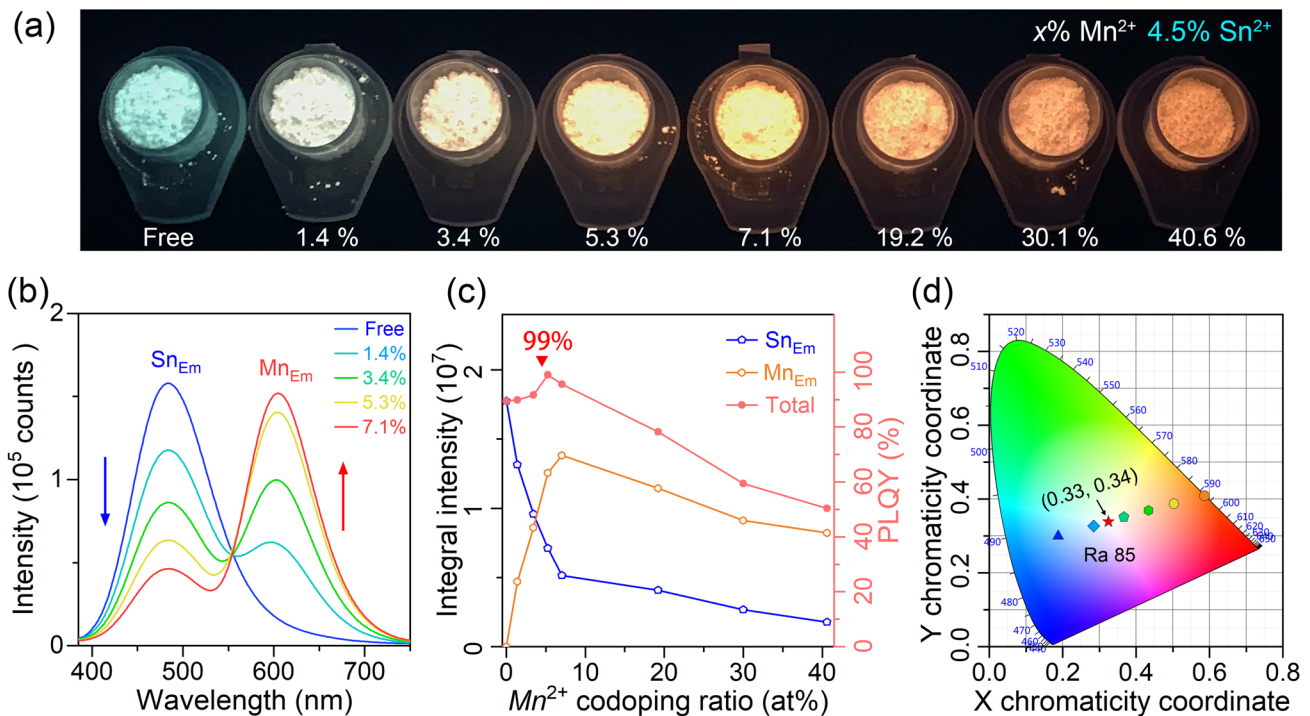


Fig. 3 **a** Optical images of Sn²⁺/Mn²⁺-co-doped samples under UV light. **b** PL spectra of Sn²⁺/Mn²⁺-co-doped samples collected using an integral sphere. **c** Integrated intensities of Sn_{Em} and Mn_{Em} components of Sn²⁺/Mn²⁺-co-doped samples with different doping ratios, and PLQYs of the dual emissions. **d** Commission Internationale de l’Eclairage (CIE) chromaticity coordinates of the Sn²⁺/Mn²⁺-co-doped samples

where I_0 is the original intensity of the cyan broadband emission of Sn²⁺-doped Rb₄CdCl₆. The revolution of Sn_{Em} intensity after Mn²⁺ co-doping agrees well with the $n=14$ relationship as shown in Fig. S11. The corresponding interaction range for the Sn²⁺ and Mn²⁺ ions is determined as ~0.9 nm, suggesting a Dexter energy transfer process. This finding further confirms the presence of exchange-coupled interaction in Sn–Mn pairs. As shown in Fig. 3d, The CIE coordinates of the PL shift from (0.19, 0.30) to (0.47, 0.38) as the Mn²⁺ concentration increases from 0 to 7.1%. The PLQY ranges from 90 to 99% and CCT ranges from 20,933 to 2,323 K. When the Mn²⁺ doping concentration is higher than 7.1%, the intensity of the Mn_{Em} component starts to decrease, but not as much as the Sn_{Em} component. As a result, the CCT of dual emission further decreased to 1,567 K. This coverage encompasses the variation range of sunlight. Notably, a CIE of (0.33, 0.34) with a CRI of up to 85 was achieved in the sample of ~3 Mn% and ~4.5 Sn% co-doped in Rb₄CdCl₆, which closely matches the standard white light required for illumination or display application.

To further investigate the thermal stability of the dual emission and gain a deeper understanding of the highly efficient energy transfer from Sn²⁺ to adjacent Mn²⁺ in

Rb₄CdCl₆ host, PL spectra were measured for Sn²⁺-doped and Sn²⁺/Mn²⁺-co-doped Rb₄CdCl₆ samples over a temperature range of 90–450 K. A pseudo-color map depicting temperature-dependent variations in PL intensity, wavelength, and FWHM is presented in Figs. 4a and S12. Both the Sn_{Em} and Mn_{Em} components exhibit a blueshift and broadening with increasing temperature. The Sn_{Em} component in the samples with and without Mn²⁺ doping shows a similar trend, providing further evidence for a short-range interaction between Sn²⁺ and Mn²⁺ ions. Based on this observation, the Mn_{Em} component was separately analyzed (Fig. S13). The integrated intensities of Sn_{Em} and Mn_{Em} as a function of temperature are shown in Fig. 4b. It is noteworthy noting that even at a temperature as high as 450 K, the Sn_{Em} and Mn_{Em} components retain 43.9% and 70.2% of their initial intensity at ambient conditions, indicating an excellent thermal stability. Conversely, as the temperature decrease to 90 K, a gradual increase in the intensity of Sn_{Em} and Mn_{Em} is observed, indicating the suppression of vibrational relaxation. These results suggest that the high energy transfer efficiency is not significantly influenced by the temperature. Figure 4b illustrates the narrowing of the Sn_{Em} and Mn_{Em}

components as the temperature decreases. The relationship between the FWHM and the temperature can be described as follows:

$$\text{FWHM}(T) = 2.36\sqrt{S\hbar\omega_{\text{phonon}}}\sqrt{\coth\frac{\hbar\omega_{\text{phonon}}}{2k_{\text{B}}T}} \quad (4)$$

where S is the Huang–Rhys factor, $\hbar\omega_{\text{phonon}}$ is the phonon frequency, and k_{B} is the Boltzmann constant [3, 14]. The S factor is a parameter that provides an estimation of the electron–phonon interaction strength by measuring the average number of vibrational quanta involved in a PL process [49]. In the case of co-doped Sn^{2+} and Mn^{2+} ions in Rb_4CdCl_6 host, we assume the same phonon frequency for both emission components. By approximating the relationship between the S factors of Sn_{Em} and Mn_{Em} using the squared ratio of their FWHM, we find that the $S_{\text{Sn}}/S_{\text{Mn}}$ value is determined to be 3–3.6. This significant difference in the

strength of the electron–phonon interaction between Sn_{Em} and Mn_{Em} could account for their distinct thermal stability.

Figure 4d and e depicts the PLE profiles of Sn_{Em} and Mn_{Em} at 90, 300, and 450 K, respectively. With increasing temperature, the PLE profiles of the two components gradually converge, as shown in Fig. S14, suggesting that the distortion caused by smaller Mn^{2+} radii becomes less significant. Interestingly, the PLE profile resembles like that of Sb^{3+} -doped $\text{Cs}_2\text{NaInCl}_6$, which has a 3D-networked structure, at high temperature, while that resembles that of Sb^{3+} -doped Rb_3InCl_6 , which has a 0D-networked structure, at low temperature (Fig. S15) [50–52]. This temperature-dependent evolution of PLE indicates the relative intensity of A and C bands is independent on structure dimensionality. The similar temperature dependence of the PLE profiles for Sn_{Em} and Mn_{Em} further confirms that the energy transfer from Sn^{2+} to Mn^{2+} in the Sn–Mn pair occurs from

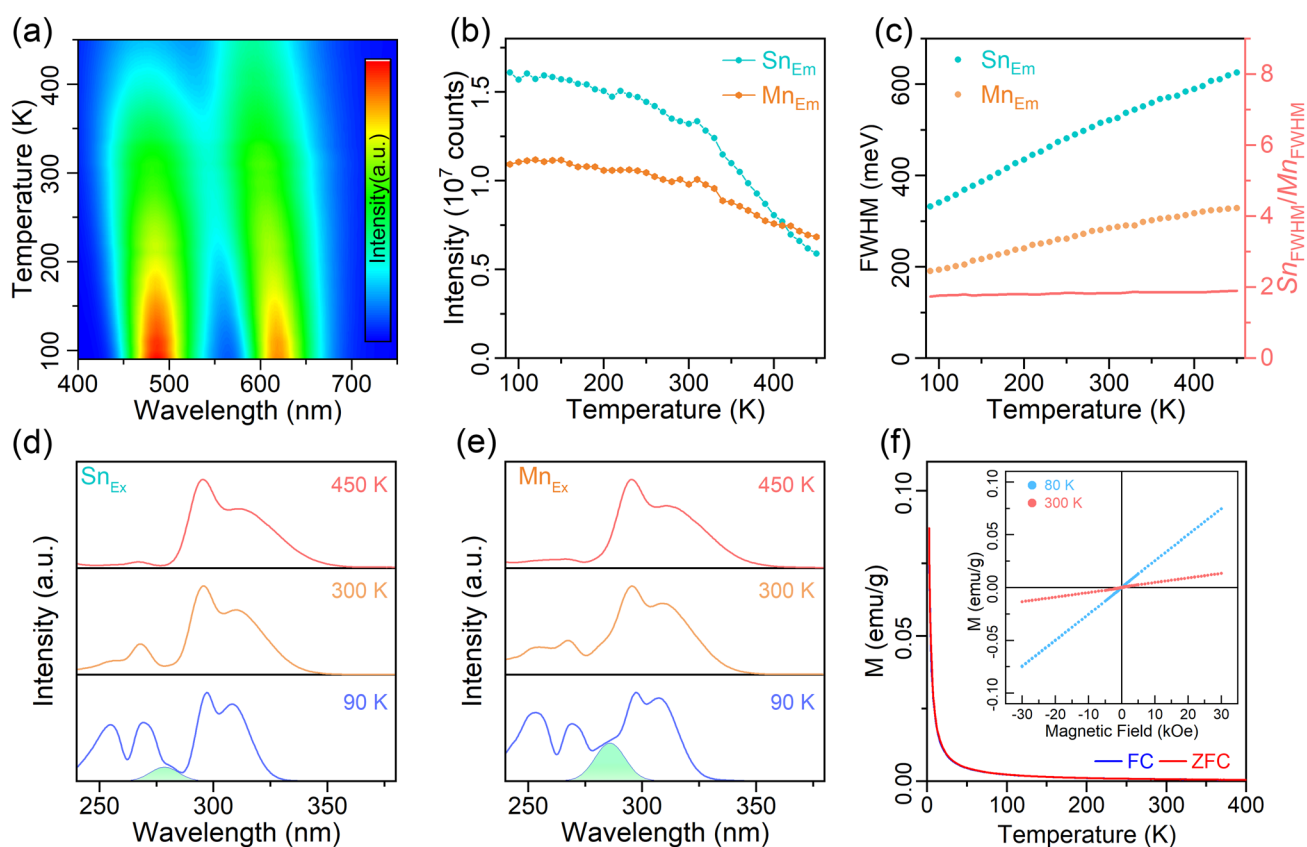


Fig. 4 **a** Pseudo-color map of the temperature-dependent PL from the $\text{Sn}^{2+}/\text{Mn}^{2+}$ -co-doped sample in the 90–450 K range. **b, c** Evolution of the integrated intensity and the FWHM with increasing temperature for Sn_{Em} and Mn_{Em} in the $\text{Sn}^{2+}/\text{Mn}^{2+}$ -co-doped sample. **d, e** Excitation profiles corresponding to Sn_{Em} and Mn_{Em} , respectively, at 90, 300, and 450 K. **f** FC and ZFC curves for the $\text{Sn}^{2+}/\text{Mn}^{2+}$ -co-doped sample. The inset shows plot hysteresis loops obtained at 80 and 300 K

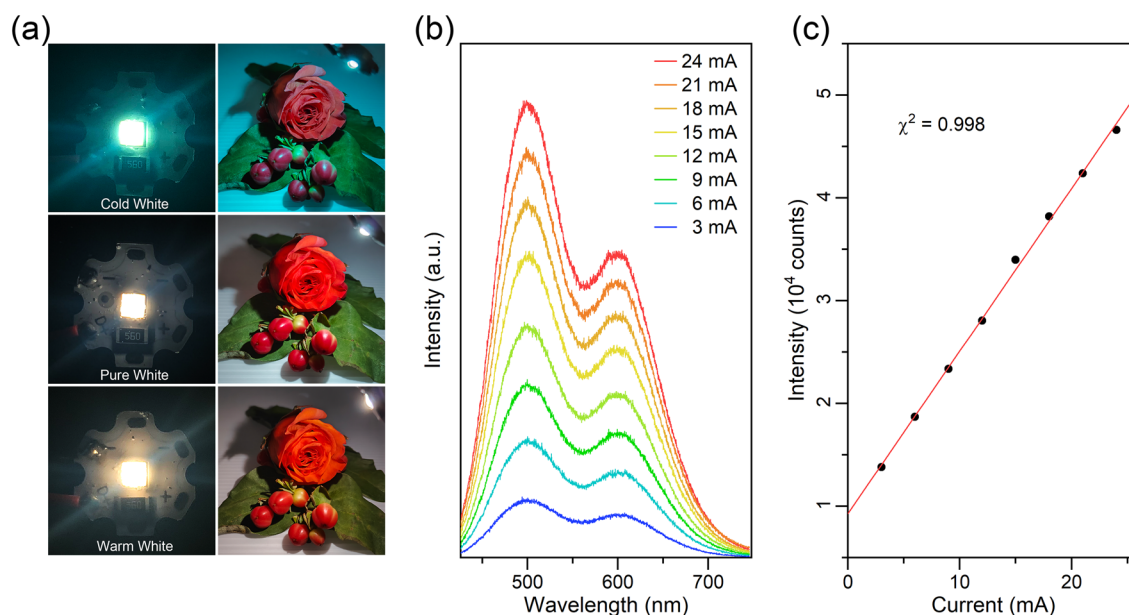


Fig. 5 **a** Fabricated down-conversion cold/warm WLEDs and the color performances of flowers under illumination by the WLEDs. **b, c** Variations in the emission spectra and the intensity of a WLED with different driving currents

the ground state rather than from the excited state [33]. To investigate whether the strong interaction between Mn^{2+} and Sn^{2+} is caused by the magnetic order of Mn^{2+} , the magnetic properties of a sample co-doped with Mn^{2+} and Sn^{2+} (3.4% and 4.5%) were examined using temperature-dependent magnetization. As shown in Fig. 4f, the zero-field-cooled (ZFC) and field-cooled (FC) curves exhibit typical paramagnetic behavior, indicating disorder of the Mn magnetic moments in the Rb_4CdCl_6 host. The absence of magnetic ordering is further supported by the observed hysteresis at 80 and 350 K of 30 kOe, as shown in the inset in Fig. 4f.

3.2 WLED Device Performance

To demonstrate the potential application of $\text{Sn}^{2+}/\text{Mn}^{2+}$ -co-doped Rb_4CdCl_6 as a single-component white emitter in lighting technology, phosphor-converting WLED devices were fabricated by directly placing the as-prepared sample powder onto a commercially available 295-nm UV chip. The fabricated WLED devices, ranging from cold to warm, are shown in Fig. 5a, along with corresponding photographs illuminated by these WLED devices. The photographs exhibit vivid and realistic colors, indicating excellent color discrimination. Figure 5b, c presents a series of emission

spectra of WLED device at different currents, with the emission intensity increases monotonously with current. The normalized emission spectra, as shown in Fig. S16, exhibit the same profile, indicating that the CRI and CCT remain relatively unchanged at different currents. These results demonstrate the good photostability of white-light device, making it suitable for practical applications.

4 Conclusions

In summary, our study successfully incorporated Sn^{2+} and Mn^{2+} ions into all-inorganic 0D Rb_4CdCl_6 perovskites, leading to the realization of near-unity and tunable dual-emission white light in a single material. The presence of short-range and strong interactions between adjacent Sn^{2+} and Mn^{2+} centers, facilitated by the formation of exchange-coupled Sn–Mn pairs, enabled highly efficient energy transfer process from Sn^{2+} as the donor to Mn^{2+} as the acceptor. The dual-emitting centers of Sn^{2+} and sensitized Mn^{2+} exhibited similar excitation profiles and could be easily adjusted by varying the Mn^{2+} doping content, allowing for precise control of the emission proportions and the generation of white light. A synchronous PL decay process observed in the dual-emission indicated stable dynamic color rendering, making it particularly advantageous for stroboscopic white-light applications. This research

provides valuable insights for the design of high-performance single-component white phosphors and diodes, opening new possibilities for next-generation lighting technologies.

Acknowledgements Y. S. acknowledges the support from the National Natural Science Foundation of China (Grant No. 61874074) and Science and Technology Project of Shenzhen (Grant No. JCYJ20220531100815034). H. L. acknowledges the support from Technology and Innovation Commission of Shenzhen (20200810164814001) and Guangdong Basic and Applied Basic Research Foundation (General Program, Grant No. 2022A1515012055).

Funding Open access funding provided by Shanghai Jiao Tong University.

Declarations

Conflict of interest The authors declare that they have no known competing financial interests or personal relationships that could have appeared to influence the work reported in this paper.

Open Access This article is licensed under a Creative Commons Attribution 4.0 International License, which permits use, sharing, adaptation, distribution and reproduction in any medium or format, as long as you give appropriate credit to the original author(s) and the source, provide a link to the Creative Commons licence, and indicate if changes were made. The images or other third party material in this article are included in the article's Creative Commons licence, unless indicated otherwise in a credit line to the material. If material is not included in the article's Creative Commons licence and your intended use is not permitted by statutory regulation or exceeds the permitted use, you will need to obtain permission directly from the copyright holder. To view a copy of this licence, visit <http://creativecommons.org/licenses/by/4.0/>.

Supplementary Information The online version contains supplementary material available at <https://doi.org/10.1007/s40820-023-01168-5>.

References

1. E.-R. Dohner, A. Jaffe, L.-R. Bradshaw, H.-I. Karunadasa, Intrinsic white-light emission from layered hybrid perovskites. *J. Am. Chem. Soc.* **136**(38), 13154–13157 (2014). <https://doi.org/10.1021/ja507086b>
2. L. Mao, Y. Wu, C.-C. Stoumpos, M.-R. Wasielewski, M.-G. Kanatzidis, White-light emission and structural distortion in new corrugated two-dimensional lead bromide perovskites. *J. Am. Chem. Soc.* **139**(14), 5210–5215 (2017). <https://doi.org/10.1021/jacs.7b01312>
3. J. Luo, X. Wang, S. Li, J. Liu, Y. Guo et al., Efficient and stable emission of warm-white light from lead-free halide double perovskites. *Nature* **563**(7732), 541–545 (2018). <https://doi.org/10.1038/s41586-018-0691-0>
4. J.-H. Wei, J.-F. Liao, L. Zhou, J.-B. Luo, X.-D. Wang et al., Indium-antimony-halide single crystals for high-efficiency white-light emission and anti-counterfeiting. *Sci. Adv.* **7**(34), eabg3989 (2021). <https://doi.org/10.1126/sciadv.abg3989>
5. Z. Yuan, C. Zhou, Y. Tian, Y. Shu, J. Messier et al., One-dimensional organic lead halide perovskites with efficient bluish white-light emission. *Nat. Commun.* **8**(1), 14051 (2017). <https://doi.org/10.1038/ncomms14051>
6. Y. Han, J. Yin, G. Cao, Z. Yin, Y. Dong et al., Exciton self-trapping for white emission in 100-oriented two-dimensional perovskites via halogen substitution. *ACS Energy Lett.* **7**(1), 453–460 (2022). <https://doi.org/10.1021/acscenergylett.1c02572>
7. M.-L. Li, Y.-P. Zhao, J. Guo, X.-Q. Qin, Q. Zhang et al., Phase regulation and defect passivation enabled by phosphoryl chloride molecules for efficient quasi-2D perovskite light-emitting diodes. *Nano-Micro Lett.* **15**, 119 (2023). <https://doi.org/10.1007/s40820-023-01089-3>
8. M. Ren, S. Cao, J. Zhao, B.-S. Zou, R.-S. Zeng, Advances and challenges in two-dimensional organic–inorganic hybrid perovskites toward high-performance light-emitting diodes. *Nano-Micro Lett.* **13**, 163 (2021). <https://doi.org/10.1007/s40820-021-00685-5>
9. J. Zhang, X. Yang, H. Deng, K.-K. Qiao, U. Farooq et al., Low-dimensional halide perovskites and their advanced optoelectronic applications. *Nano-Micro Lett.* **9**, 36 (2017). <https://doi.org/10.1007/s40820-017-0137-5>
10. Q. Guo, X. Zhao, B. Song, J. Luo, J. Tang, Light emission of self-trapped excitons in inorganic metal halides for optoelectronic applications. *Adv. Mater.* **34**(52), 2201008 (2022). <https://doi.org/10.1002/adma.202201008>
11. H. Yuan, F. Massuyeau, N. Gautier, A.-B. Kama, E. Faulques et al., Doped lead halide white phosphors for very high efficiency and ultra-high color rendering. *Angew. Chem. Int. Ed.* **59**(7), 2802–2807 (2020). <https://doi.org/10.1002/anie.201910180>
12. D. Zhao, G. Xiao, Z. Liu, L. Sui, K. Yuan et al., Harvesting cool daylight in hybrid organic–inorganic halides microtubules through the reservation of pressure-induced emission. *Adv. Mater.* **33**(31), 2100323 (2021). <https://doi.org/10.1002/adma.202100323>
13. R. Fu, W. Zhao, L. Wang, Z. Ma, G. Xiao et al., Pressure-induced emission toward harvesting cold white light from warm white light. *Angew. Chem. Int. Ed.* **60**(18), 10082–10088 (2021). <https://doi.org/10.1002/anie.202015395>
14. S. Li, J. Luo, J. Liu, J. Tang, Self-trapped excitons in all-inorganic halide perovskites: fundamentals, status, and potential applications. *J. Phys. Chem. Lett.* **10**(8), 1999–2007 (2019). <https://doi.org/10.1021/acs.jpcclett.8b03604>
15. Z. Ma, Z. Shi, D. Yang, Y. Li, F. Zhang et al., High color-rendering index and stable white light-emitting diodes by assembling two broadband emissive self-trapped excitons.

- Adv. Mater. **33**(2), 2001367 (2021). <https://doi.org/10.1002/adma.202001367>
16. B. Zhou, Z.-X. Liu, H.-N. Li, S.-F. Fang, F.-E. Fang et al., Highly efficient white-light emission triggered by Sb^{3+} dopant in indium-based double perovskites. *Adv. Photonics Res.* **2**(12), 2100143 (2021). <https://doi.org/10.1002/adpr.202100143>
 17. J. Nie, B. Zhou, S. Fang, Y. Wang, Y. Wang et al., Chemical doping of lead-free metal-halide-perovskite related materials for efficient white-light photoluminescence. *Mater. Today Phys.* **31**, 100992 (2023). <https://doi.org/10.1016/j.mtphys.2023.100992>
 18. K.-P. Lindquist, M.-A. Boles, S.A. Mack, J.-B. Neaton, H.-I. Karunadasa, Gold-cage perovskites: a three-dimensional $\text{Au}^{\text{III}}-\text{X}$ framework encasing isolated MX_6^{3-} octahedra ($\text{M}^{\text{III}} = \text{In, Sb, Bi}$; $\text{X} = \text{Cl}^-, \text{Br}^-, \text{I}^-$). *J. Am. Chem. Soc.* **143**(19), 7440–7448 (2021). <https://doi.org/10.1021/jacs.1c01624>
 19. C.-M. Dai, T. Zhang, Y.-N. Wu, S.-Y. Chen, Halide double-perovskite light-emitting centers embedded in lattice-matched and coherent crystalline matrix. *Adv. Funct. Mater.* **30**(17), 2000653 (2020). <https://doi.org/10.1002/adfm.202000653>
 20. Z.-C. Zeng, B.-L. Huang, X. Wang, L. Lu, Q.-Y. Lu et al., Multimodal luminescent $\text{Yb}^{3+}/\text{Er}^{3+}/\text{Bi}^{3+}$ -doped perovskite single crystals for X-ray detection and anti-counterfeiting. *Adv. Mater.* **32**(43), 2004506 (2020). <https://doi.org/10.1002/adma.202004506>
 21. L. Chu, W. Ahmad, W. Liu, J. Yang, R. Zhang et al., Lead-free halide double perovskite materials: a new superstar toward green and stable optoelectronic applications. *Nano-Micro Lett.* **11**(1), 16 (2019). <https://doi.org/10.1007/s40820-019-0244-6>
 22. Q.-Q. Fan, G.-V. Biesold-McGee, J.-Z. Ma, Q.-N. Xu, S. Pan et al., Lead-free halide perovskite nanocrystals: crystal structures, synthesis, stabilities, and optical properties. *Angew. Chem. Int. Ed.* **59**(3), 1030–1046 (2020). <https://doi.org/10.1002/anie.201904862>
 23. D.-W. Duan, C.-Y. Ge, M.-Z. Rahaman, C.-H. Lin, Y.-M. Shi et al., Recent progress with one-dimensional metal halide perovskites: from rational synthesis to optoelectronic applications. *NPG Asia Mater.* **15**(1), 8 (2023). <https://doi.org/10.1038/s41427-023-00465-0>
 24. B. Zhou, Z.-X. Liu, S.-F. Fang, H.-Z. Zhong, B.-B. Tian et al., Efficient white photoluminescence from self-trapped excitons in $\text{Sb}^{3+}/\text{Bi}^{3+}$ -codoped $\text{Cs}_2\text{NaInCl}_6$ double perovskites with tunable dual-emission. *ACS Energy Lett.* **6**(9), 3343–3351 (2021). <https://doi.org/10.1021/acsenergylett.1c01442>
 25. S.-F. Gong, R.-R. Wu, S. Yang, L.-F. Wu, M.-M. Zhang et al., Tuning the luminous properties and optical thermometry of Cs_2SnCl_6 phosphor microcrystals via Bi and Sb codoping. *Photonics Res.* **9**(11), 2182 (2021). <https://doi.org/10.1364/PRJ.431672>
 26. Y. Zhong, Y.-E. Huang, T. Deng, Y.-T. Lin, X.-Y. Huang et al., Multi-dopant engineering in perovskite Cs_2SnCl_6 : white light emitter and spatially luminescent heterostructure. *Inorg. Chem.* **60**(22), 17357–17363 (2021). <https://doi.org/10.1021/acs.inorgchem.1c02840>
 27. W. Zhang, W. Zheng, L.-Y. Li, P. Huang, Z.-L. Gong et al., Dual-band-tunable white-light emission from $\text{Bi}^{3+}/\text{Te}^{4+}$ emitters in perovskite-derivative Cs_2SnCl_6 microcrystals. *Angew. Chem. Int. Ed.* **134**(9), e202116085 (2022). <https://doi.org/10.1002/ange.202116085>
 28. B. Chen, Y. Guo, Y. Wang, Z. Liu, Q. Wei et al., Multiexcitonic emission in zero-dimensional $\text{Cs}_2\text{ZrCl}_6:\text{Sb}^{3+}$ perovskite crystals. *J. Am. Chem. Soc.* **143**(42), 17599–17606 (2021). <https://doi.org/10.1021/jacs.1c07537>
 29. F. Zhang, X. Chen, X.-F. Qi, W.-Q. Liang, M. Wang et al., Regulating the singlet and triplet emission of Sb^{3+} ions to achieve single-component white-light emitter with record high color-rendering index and stability. *Nano Lett.* **22**(12), 5046–5054 (2022). <https://doi.org/10.1021/acs.nanolett.2c00733>
 30. C.-Y. Huang, H.-C. Li, Y. Wu, C.-H. Lin, X.-W. Guan et al., Inorganic halide perovskite quantum dots: a versatile nanomaterial platform for electronic applications. *Nano-Micro Lett.* **15**(1), 16 (2023). <https://doi.org/10.1007/s40820-022-00983-6>
 31. A. Nocolak, V. Morad, K.-M. McCall, S. Yakunin, Y. Shynkarenko et al., Bright blue and green luminescence of $\text{Sb}(\text{III})$ in double perovskite $\text{Cs}_2\text{MInCl}_6$ ($\text{M} = \text{Na, K}$) matrices. *Chem. Mater.* **32**(12), 5118–5124 (2020). <https://doi.org/10.1021/acs.chemmater.0c01004>
 32. H. Arfin, A.-S. Kshirsagar, J. Kaur, B. Mondal, Z.-G. Xia et al., Ns^2 electron (Bi^{3+} and Sb^{3+}) doping in lead-free metal halide perovskite derivatives. *Chem. Mater.* **32**(24), 10255–10267 (2020). <https://doi.org/10.1021/acs.chemmater.0c03394>
 33. S. Saikia, A. Joshi, H. Arfin, S. Badola, S. Saha et al., $\text{Sb}^{3+}-\text{Er}^{3+}$ -codoped $\text{Cs}_2\text{NaInCl}_6$ for emitting blue and short-wave infrared radiation. *Angew. Chem. Int. Ed.* **61**(32), e202201628 (2022). <https://doi.org/10.1002/anie.202201628>
 34. J.-H. Nie, B. Zhou, S.-F. Fang, H.-Z. Zhong, H.-N. Li et al., Efficient multicolor and white photoluminescence in erbium- and holmium-incorporated $\text{Cs}_2\text{NaInCl}_6:\text{Sb}^{3+}$ double perovskites. *Chem. Mater.* **34**(14), 6288–6295 (2022). <https://doi.org/10.1021/acs.chemmater.2c00333>
 35. B.-B. Su, G.-J. Zhou, J.-L. Huang, E.-H. Song, A. Nag et al., Mn^{2+} -doped metal halide perovskites: structure, photoluminescence, and application. *Laser Photonics Rev.* **15**(1), 2000334 (2021). <https://doi.org/10.1002/lpor.202000334>
 36. V. Pinchetti, F. Moro, B. Zhang, M. Fanciulli, L. De Trizio et al., Magnetic transitions and energy transfer processes in Sb-based zero-dimensional metal halide nanocrystals doped with manganese. *ACS Energy Lett.* **7**(4), 1566–1573 (2022). <https://doi.org/10.1021/acsenergylett.2c00364>
 37. X.Y. Liu, X. Xu, B. Li, L.-L. Yang, Q. Li et al., Tunable dual-emission in monodispersed $\text{Sb}^{3+}/\text{Mn}^{2+}$ codoped $\text{Cs}_2\text{NaInCl}_6$ perovskite nanocrystals through an energy transfer process. *Small* **16**(31), 2002547 (2020). <https://doi.org/10.1002/sml.202002547>
 38. H.-L. Yuan, L. Qi, Y.M. Paris, F. Chen, Q. Shen et al., Machine learning guided design of single-phase hybrid lead halide white phosphors. *Adv. Sci.* **8**(19), 2101407 (2021). <https://doi.org/10.1002/advs.202101407>



39. M. Gao, Y.-X. Pan, C.-D. Peng, Y.-H. Ding, H.-Z. Lian et al., White light emission from single-component $\text{Cs}_7\text{Cd}_3\text{Br}_13:\text{P}^{\text{b}2+}$, $\text{M}^{\text{n}2+}$ crystals with high quantum efficiency and enhanced thermodynamic stability. *Chem. Mater.* **35**, 773–782 (2023). <https://doi.org/10.1021/acs.chemmater.2c03560>
40. S.-M. Bai, P. Zhang, P. Antoniou, S.-S. Skourtis, D.-N. Beratan, Quantum interferences among Dexter energy transfer pathways. *Faraday Discuss.* **216**, 301–318 (2019). <https://doi.org/10.1039/C9FD00007K3>
41. B. Zhou, D. Ding, Y. Wang, S.-F. Fang, Z.-X. Liu et al., A scalable H_2O –DMF–DMSO solvent synthesis of highly luminescent inorganic perovskite-related cesium lead bromides. *Adv. Opt. Mater.* **9**(3), 2001435 (2021). <https://doi.org/10.1002/adom.202001435>
42. J.-C. Jin, Y.-H. Peng, Y.-T. Xu, K. Han, A.-R. Zhang et al., Bright green emission from self-trapped excitons triggered by Sb^{3+} doping in Rb_4CdCl_6 . *Chem. Mater.* **34**(12), 5717–5725 (2022). <https://doi.org/10.1021/acs.chemmater.2c01254>
43. J.-L. Yao, C. Cao, H.-M. Cheng, D.-Y. Wang, W.-S. Yang et al., All-inorganic zero-dimensional Sn-doped Rb_4CdCl_6 with near-unity quantum efficiency. *J. Phys. Chem. C* **127**(7), 3602–3608 (2023). <https://doi.org/10.1021/acs.jpcc.2c08483>
44. N. Wang, Y. Xiong, K.-J. Liu, S.-H. He, J.-D. Cao et al., Efficient narrow-band green light-emitting hybrid halides for wide color gamut display. *ACS Appl. Electron. Mater.* **4**(8), 4068–4076 (2022). <https://doi.org/10.1021/acsaelm.2c00705>
45. W. Zheng, X.-L. Li, N.-Q. Liu, S. Yan, X.-J. Wang et al., Solution-grown chloride perovskite crystal of red afterglow. *Angew. Chem. Int. Ed.* **60**(46), 24450–24455 (2021). <https://doi.org/10.1002/anie.202110308>
46. C. Li, Z.-S. Luo, Y.-L. Liu, Y. Wei, X. He et al., Self-trapped exciton emission with high thermal stability in antimony-doped hybrid manganese chloride. *Adv. Opt. Mater.* **10**(12), 2102746 (2022). <https://doi.org/10.1002/adom.202102746>
47. D.-X. Zhu, M.-L. Zaffalon, J. Zito, F. Cova, F. Meinardi et al., Sb-doped metal halide nanocrystals: a 0D versus 3D comparison. *ACS Energy Lett.* **6**(6), 2283–2292 (2021). <https://doi.org/10.1021/acsenergylett.1c00789>
48. B. Zhou, Z.-X. Liu, S.-F. Fang, J.-H. Nie, H.-Z. Zhong et al., Emission mechanism of self-trapped excitons in Sb^{3+} -doped all-inorganic metal-halide perovskites. *J. Phys. Chem. Lett.* **13**(39), 9140–9147 (2022). <https://doi.org/10.1021/acs.jpcclett.2c02759>
49. M. de Jong, L. Seijo, A. Meijerink, F.-T. Rabouw, Resolving the ambiguity in the relation between stokes shift and Huang–Rhys parameter. *Phys. Chem. Chem. Phys.* **17**(26), 16959–16969 (2015). <https://doi.org/10.1039/C5CP02093J>
50. R.-S. Zeng, L.-L. Zhang, Y. Xue, B. Ke, Z. Zhao et al., Highly efficient blue emission from self-trapped excitons in stable Sb^{3+} -doped $\text{Cs}_2\text{NaInCl}_6$ double perovskites. *J. Phys. Chem. Lett.* **11**(6), 2053–2061 (2020). <https://doi.org/10.1021/acs.jpcclett.0c00330>
51. P.-G. Han, C. Luo, S.-Q. Yang, Y. Yang, W.-Q. Deng et al., All-inorganic lead-free 0D perovskites by a doping strategy to achieve a PLQY boost from < 2 to 90%. *Angew. Chem. Int. Ed.* **132**(31), 12809–12813 (2020). <https://doi.org/10.1002/ange.202003234>
52. J.-D. Majher, M.-B. Gray, T. Liu, N.-P. Holzapfel, P.-M. Woodward, Rb_3InCl_6 : a monoclinic double perovskite derivative with bright Sb^{3+} -activated photoluminescence. *Inorg. Chem.* **59**(19), 14478–14485 (2020). <https://doi.org/10.1021/acs.inorgchem.0c02248>